

Ammonia Borane Dehydrogenation Catalyzed by $(\kappa^4\text{-EP}_3)\text{Co}(\text{H})$ [$\text{EP}_3 = \text{E}(\text{CH}_2\text{CH}_2\text{PPh}_2)_3$; $\text{E} = \text{N}, \text{P}$] and H_2 Evolution from Their Interaction with NH Acids

Stefano Todisco,[†] Lapo Luconi,[†] Giuliano Giambastiani,^{†,§} Andrea Rossin,^{*,†} Maurizio Peruzzini,[†] Igor E. Golub,^{‡,||} Oleg A. Filippov,^{‡,||} Natalia V. Belkova,^{‡,||} and Elena S. Shubina^{*,‡}

[†]Istituto di Chimica dei Composti Organometallici–Consiglio Nazionale delle Ricerche (ICCOM - CNR), Via Madonna del Piano 10, 50019, Sesto Fiorentino, Italy

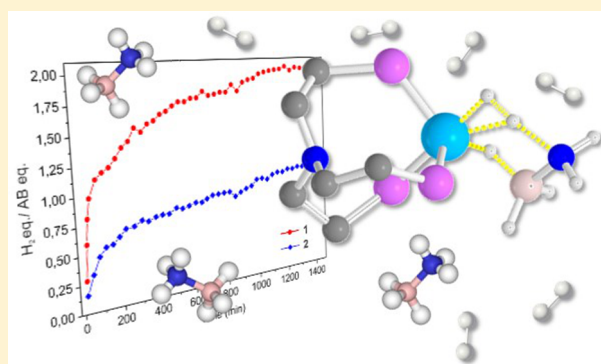
[‡]A.N. Nesmeyanov Institute of Organoelement Compounds, Russian Academy of Sciences (INEOS RAS), Vavilova Street 28, 119991 Moscow, Russia

[§]Kazan Federal University, Kremlyovskaya Street 18, 420008 Kazan, Russia

^{||}People's Friendship University of Russia (RUDN University), 6 Miklukho-Maklay St., 117198 Moscow, Russia

Supporting Information

ABSTRACT: Two Co(I) hydrides containing the tripodal polyphosphine ligand EP_3 , $(\kappa^4\text{-EP}_3)\text{Co}(\text{H})$ [$\text{E}(\text{CH}_2\text{CH}_2\text{PPh}_2)_3$; $\text{E} = \text{N}$ (**1**), P (**2**)], have been exploited as ammonia borane (NH_3BH_3 , AB) dehydrogenation catalysts in THF solution at $T = 55$ °C. The reaction has been analyzed experimentally through multinuclear (^{11}B , $^{31}\text{P}\{^1\text{H}\}$, ^1H) NMR and IR spectroscopy, kinetic rate measurements, and kinetic isotope effect (KIE) determination with deuterated AB isotopologues. Both complexes are active in AB dehydrogenation, albeit with different rates and efficiency. While **1** releases 2 equiv of H_2 per equivalent of AB in ca. 48 h, with concomitant borazine formation as the final “spent fuel”, **2** produces 1 equiv of H_2 only per equivalent of AB in the same reaction time, along with long-chain poly(aminoboranes) as insoluble byproducts. A DFT modeling of the first AB dehydrogenation step has been performed, at the M06//6-311++G** level of theory. The combination of the kinetic and computational data reveals that a simultaneous B–H/N–H activation occurs in the presence of **1**, after a preliminary AB coordination to the metal center. In **2**, no substrate coordination takes place, and the process is better defined as a sequential BH_3/NH_3 insertion process on the initially formed $[\text{Co}]\text{-NH}_2\text{BH}_3$ amidoborane complex. Finally, the reaction of **1** and **2** with NH -acids [AB and Me_2NHBH_3 (DMAB)] has been followed via VT-FTIR spectroscopy (in the -80 to $+50$ °C temperature range), with the aim of gaining a deeper experimental understanding of the dihydrogen bonding interactions that are at the origin of the observed H_2 evolution.



INTRODUCTION

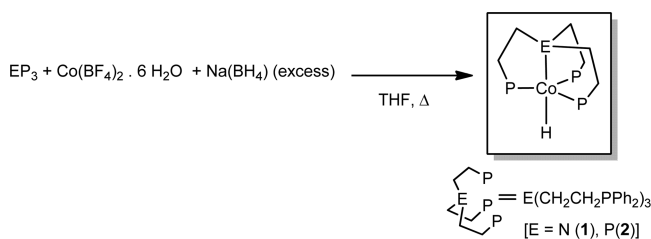
Chemical hydrogen storage, i.e., the possibility to release molecular H_2 on demand from hydrogen-rich, light, and safe compounds, has become a challenging research area in the past decade.¹ Under this perspective, chemical compounds that are easy-to-handle, thermally stable, and with a relatively high hydrogen content are in the spotlight of contemporary chemical hydrogen storage research. One of the most studied inorganic materials is ammonia borane (NH_3BH_3 , AB),² with a maximum hydrogen content of 19.3 wt %. Homogeneously catalyzed AB dehydrogenation has become increasingly popular in the recent organometallic chemistry literature, where H_2 evolution is mediated by organometallics of the elements from the second and third transition series.³ The exploitation of 4d or 5d metals helps with the stabilization of reaction intermediates, allowing for their isolation and thorough

characterization. Nevertheless, when considering practical applications (such as the transportation sector), these metals are unsuitable because of their low natural abundance and high cost. The choice of more cost-effective and earth-abundant 3d elements (like titanium,⁴ chromium,⁵ manganese,⁶ iron,⁷ or nickel⁸) represents the new frontier in this research area. Within the 3d series, cobalt is one of the least exploited. To date, only one example of a cobalt(I) (PBP) pincer complex has been shown to catalyze AB dehydrogenation with satisfactory rates at room temperature and with the production of 1 equiv of H_2 per monomer.⁹ Besides pincer backbones, another class of robust ligands is that of the potentially tetradentate $\text{E}(\text{CH}_2\text{CH}_2\text{PPh}_2)_3$ (EP_3 ; $\text{E} = \text{N}, \text{P}$). EP_3 ligands

Received: November 6, 2016

offer a diversity of coordination geometries, showing varied κ^4 -, κ^3 -, and κ^2 -coordination hapticities.¹⁰ The presence of the E donor and of ethylene spacers separating the phosphorus donors from the bridgehead atom makes EP₃ more flexible than other tripodal polyphosphines, e.g., MeC(CH₂PPh₂)₃ (triphos), increasing at the same time the overall basicity at the metal center.^{10,11} Following our previous investigations on NP₃-containing ruthenium polyhydrides as AB dehydrogenation catalysts,¹² two cobalt hydrides (κ^4 -NP₃)Co(H) (**1**) and (κ^4 -PP₃)Co(H) (**2**) (Scheme 1) have been exploited for the same

Scheme 1. Synthesis of the EP₃ Co(I) Hydrides **1** and **2**^a



^aSee refs 14 and 15 for details.

task, at $T = 55$ °C. Their reaction with AB in catalytic regimes has been followed experimentally [multinuclear ¹¹B, ³¹P{¹H}], ¹H NMR and IR spectroscopy, kinetic rate measurements, and kinetic isotope effect (KIE) studies through the employment of deuterated AB isotopologues] and modeled computationally (DFT//M06//6-311++G** modeling of the first dehydrogenation step). The interaction of **1** and **2** with AB and Me₂NHBH₃ (DMAB) has been examined under stoichiometric conditions using variable-temperature IR spectroscopy (VT-FTIR), to gain a deeper understanding of the dihydrogen bonding (DHB) interactions that are at the origin of the observed H₂ evolution.

EXPERIMENTAL SECTION

General Considerations. All reactions were performed using standard Schlenk procedures under a dry nitrogen atmosphere. The NP₃ ligand,¹³ **1**,¹⁴ **2**,¹⁵ NH₃BD₃, ND₃BH₃, and ND₃BD₃¹⁶ were prepared according to the published procedures. Commercial reagents (PP₃, ammonia borane, dimethylamine borane, sodium borohydride, cobalt tetrafluoroborate hexahydrate [Co(BF₄)₂·6H₂O]) were purchased from Aldrich and used as received, without further purification. Tetrahydrofuran (THF) and toluene were purified by standard distillation techniques. THF-*d*₈ (Aldrich) was stored over 4 Å molecular sieves and degassed by three freeze–pump–thaw cycles before use. NMR spectra were recorded on a BRUKER AVANCE II 300 spectrometer. ¹H and ¹³C{¹H} chemical shifts are reported in parts per million (ppm) downfield of tetramethylsilane (TMS) and were calibrated against the residual resonance of the deuterated solvent, while ³¹P{¹H} chemical shifts were referenced to 85% H₃PO₄ with downfield shift taken as positive. ¹¹B and ¹¹B{¹H} were referenced to BF₃·OEt₂. FTIR spectra in the solid state (KBr pellets) were recorded on a PerkinElmer Spectrum BX Series FTIR spectrometer, in the 4000–400 cm^{−1} range, with a 2 cm^{−1} resolution.

NMR Monitoring of the Reactions of **1 and **2** with AB.** A quartz 5 mm NMR tube was loaded with 30 mg of **1** (molecular mass = 713.65 u, 0.042 mmol) or 31 mg of **2** (molecular mass = 730.62 u, 0.042 mmol) under an inert atmosphere, and then 0.3 mL of dry and degassed THF-*d*₈ was transferred into the tube via cannula, under nitrogen. The solution obtained was first used to record the ¹H and ³¹P{¹H} NMR spectra of the catalysts. The reactions with AB were monitored as follows: 5 equiv of AB was dissolved in 0.2 mL of THF-*d*₈ in a separate Schlenk flask under nitrogen, and the resulting solution

was syringed into the NMR tube containing the hydride sample, at 25 °C. The temperature was slowly raised to 55 °C within the NMR spectrometer probe head, and new sets of multinuclear ¹H, ³¹P{¹H}, and ¹¹B NMR data were collected at that temperature for a total analysis time of 24 h.

Kinetic Measurements. The H₂ production during the reaction of AB with **1** or **2** in THF was monitored through the Man of the Moon X102 kit [see Figure S1 of the Supporting Information (SI) for details]. In a typical experiment, 26 mg of **1** (0.036 mmol) or 28 mg of **2** (0.038 mmol) were placed under an inert atmosphere in a two-necked round-bottomed 30 mL flask connected to a switchable three-way valve through a Torton screw. The solid was dissolved in 3 mL of THF; then, a total amount of 15 equiv of solid AB was added to the catalyst solution. The as-obtained mixture was brought to 55 °C in a water/oil bath under stirring, and then the valve was switched to the pressure transducer which is wirelessly connected to the software recording the kinetic profile online for a total time of 24 h. The resulting kinetic data were corrected by the vapor pressure of pure THF at the same temperature recorded on a blank solution; the pressure increase caused by THF was used to calculate the correct number of released H₂ equivalents. The calculation was made by assuming ideality for hydrogen gas, applying the $PV = nRT$ ideal gas law. At the end of the reaction, the supernatant was transferred to an NMR tube and analyzed through ¹¹B NMR spectroscopy, to identify the soluble reaction byproducts. In the case of **2**, the insoluble residue obtained after 24 h was washed twice with degassed pentane and dried under vacuum before recording the IR spectrum (KBr).

Variable-Temperature Infrared (VT-IR) Measurements. Variable-temperature IR studies were carried out on FTIR Shimadzu IR Prestige-21 spectrometer using 0.04–0.22 cm CaF₂ cells in the −80 to +50 °C temperature range using a home-modified cryostat (Carl Zeiss Jena). The accuracy of the experimental temperature was ±0.5 °C. The cryostat modification allows for transfer of the reagents (premixed at either low or room temperature) under an inert atmosphere directly into the cells.

Computational Details. Density functional theory (DFT) calculations were performed using the Gaussian09 program (revision C.01).¹⁷ Model structures were optimized with a M06 functional¹⁸ (already employed successfully in other cases for the treatment of molecules containing dative bonds¹⁹) using the SDD/D95 pseudopotential and a related basis set²⁰ on the cobalt and phosphorus atoms, a 6-31G* basis set on the C atoms, and a 6-311++G** basis set on the B, N, and H atoms. The introduction of diffuse functions is essential to well-reproduce conformational equilibria and experimental electron affinities.²¹ An extra d-type polarization function for P and an extra f-type function for Co were added to the standard set.²² Gibbs energy calculations to infer relative thermodynamic stabilities were carried out on a model system. The initially guessed geometry for the optimization was obtained starting from the XRD structures of **1** and **2** and by replacing the phenyl groups on the NP₃ ligand with H atoms (^HNP₃), in order to reach a satisfactory compromise between model system accuracy and short computational times. IRC analysis²³ was performed to find the two minima linked by the related transition structure. When IRC calculations failed to reach the minima, geometry optimizations from the initial phase of the IRC path were performed. Frequency calculations were made on all the optimized structures, to characterize the stationary points as minima or transition states (TSS), as well for the calculation of zero-point energies, enthalpies, entropies, and gas-phase Gibbs energies at 298 K. Evaluation of the solvent effects was performed through a continuum modeling of the reaction medium. Bulk solvent effects (THF, $\epsilon = 7.42$) were expressed through the SMD continuum model,²⁴ with the same basis set used for the gas-phase optimizations. Gibbs energy in solution was calculated according to the following simplified equation: $G_{\text{THF}} = G_{\text{gas}} + (E_{\text{THF}} - E_{\text{gas}})$.

RESULTS AND DISCUSSION

Characterization of Hydrides. The classical Co(I) hydrides **1** and **2** were straightforwardly prepared following the literature procedures^{14,15} from a mixture of cobalt(II)

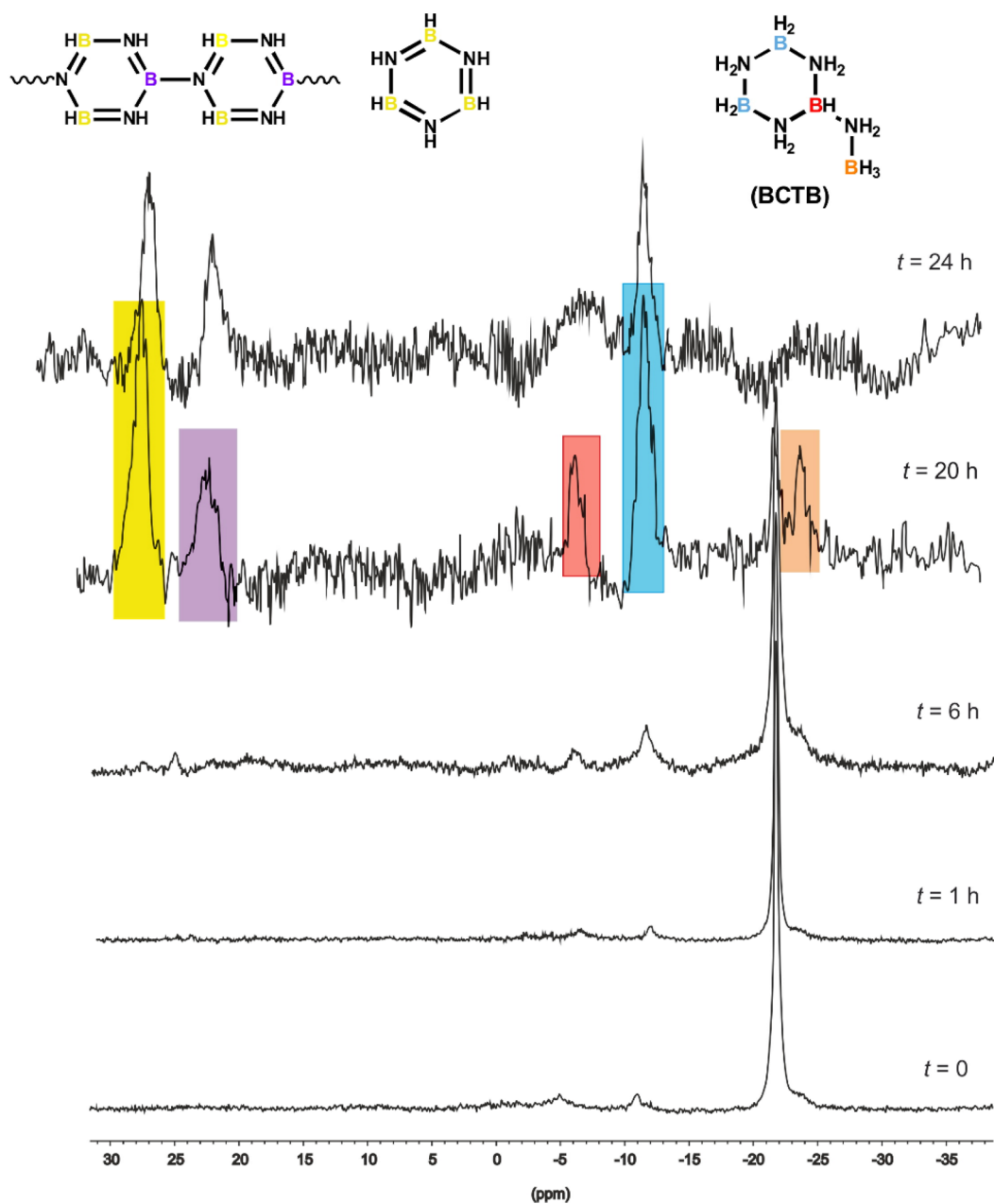


Figure 1. Typical $^{11}\text{B}\{^1\text{H}\}$ NMR spectra evolution over time of the 1:AB mixtures (1:3 stoichiometric ratio) in $\text{THF-}d_8$ at $T = 55^\circ\text{C}$.

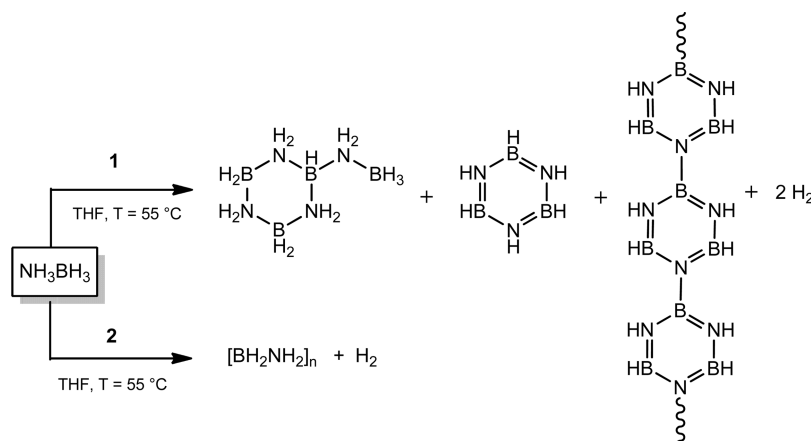
tetrafluoroborate hydrate and EP_3 in the presence of an excess (2–4 equiv) of a reducing agent (NaBH_4) at $T = 50^\circ\text{C}$, in acetone/ethanol (Scheme 1). A full and detailed multinuclear NMR characterization has already been reported for the PP_3^- -containing species **2**,²⁵ while it is missing for the NP_3 analogue **1**. Therefore, we report it herein for the sake of completeness. In $\text{THF-}d_8$ at 25°C , the bright-red compound ($\kappa^4\text{-NP}_3$)Co(H) features ^1H and $^{31}\text{P}\{^1\text{H}\}$ NMR spectra that show a broad quartet centered at $\delta_{\text{H}} = -25.7$ ppm in the hydride zone ($^2J_{\text{H-P}} = 45.4$ Hz, Figure S2, SI) and a singlet at $\delta_{\text{P}} = 54.1$ ppm (Figure S3, SI) respectively, as expected for a five-coordinated cobalt center in a trigonal bipyramidal coordination geometry. The three P atoms are magnetically and chemically equivalent, lying on the equatorial plane of the bipyramid. The IR spectra of **1** and **2** dissolved in THF feature one broad ν_{CoH} band (1798 cm^{-1} for **1** and 1795 cm^{-1} for **2**), which is unsymmetrical due

to the superposition with aromatic overtones also present in this spectral region.

Reactions of **1** and **2** with Ammonia Borane and Determination of the Kinetic Parameters for **1**.

Complexes **1** and **2** were exploited as homogeneous catalysts for AB dehydrogenation, and the process was followed through multinuclear NMR spectroscopy combined with the quantitative determination of the H_2 produced in the process. Dehydrogenation occurs at an appreciable rate only at 55°C ; no H_2 production is observed at ambient temperature, as witnessed by the absence of any appreciable change in the NMR spectra of the reagents mixture. Hydrogen evolution (seen as a sharp singlet at $\delta_{\text{H}} = 4.6$ ppm in the ^1H NMR spectra) was recorded for both **1** and **2**, albeit with different efficiency and rates. In both cases, the starting classical hydride was the only chemical species detected in the ^1H and $^{31}\text{P}\{^1\text{H}\}$ NMR spectra at all times. For **1**, ca. 2 equiv of H_2 per

Scheme 2. Catalytic AB Dehydrogenation with 1 and 2 as Homogeneous Catalysts



equivalent of AB can be produced, together with the byproducts deriving from the monomer oligomerization observed in the $^{11}\text{B}\{^1\text{H}\}$ NMR spectra [the cyclic tetramer *B*-(cyclotriborazanyl)-amine-borane (BCTB), borazine, and polyborazynes; see Figure 1 and Scheme 2].^{1e,2b,26,7a} Given the 2:1 intensity ratio of the two signals at $\delta_{\text{B}} = -13.2$ (triplet on the ^{11}B spectrum, “ BH_2N_2 ” boron chemical surrounding) and -7.2 ppm (doublet on ^{11}B , “ BHN_3 ”), the aminoborane trimer cyclotriborazane ($\text{B}_3\text{N}_3\text{H}_{12}$) may also be present in solution.

As for 2, the amount of H_2 produced is lower (1 equiv of H_2 per equivalent of AB). An insoluble BN-containing product is the final reaction outcome, identified as linear/branched poly(aminoboranes) of general formula $[\text{BH}_2\text{NH}_2]_n$, as judged from the typical $\nu(\text{NH}_2)/\nu(\text{BH}_2)/\nu(\text{BN})$ bands of the IR spectrum of the solid precipitate [Figure S4 (SI) and Scheme 2].²⁷ In the $^{11}\text{B}\{^1\text{H}\}$ NMR spectrum of the reaction mixture (Figure S5, SI), there are only few traces of the soluble fraction of the poly(aminoboranes) byproduct. The difference in the catalytic outcome of the two hydrides allows for their classification as type II (1) and type I (2) transition-metal catalysts, respectively, according to the criterion recently proposed by Paul and co-workers based on previous studies of Baker and co-workers.²⁸ Figure 2 shows the kinetic profiles of the two catalysts obtained through volumetric measurements of the amount of H_2 produced over time (see the Experimental Section), for a total reaction time of 24 h. It is clear that the H_2 equivalents produced by 1 are doubled when compared with

those produced by 2. In addition, in the case of 1 it was found that the increase of H_2 pressure in the closed vessel as long as the catalysis proceeds is detrimental, causing a significant reduction of the reaction rate. This finding is in line with the hypothetical formation of a transient dihydrogen complex as a catalytic intermediate (see the section on DFT analysis below). H_2 “overpressure” had no effect on the catalytic performance of 2. The amount of H_2 produced and the related catalyst efficiency of 1 is higher than that of $(\text{PBP})\text{Co}(\text{N}_2)$,⁹ while that of 2 is comparable to that of $(\text{PBP})\text{Co}(\text{N}_2)$ (albeit 2 works at higher temperatures and for longer reaction times). The behavior of 1 is very similar to that reported for the ruthenium analogue $(\kappa^4\text{-NP}_3)\text{Ru}(\text{H})_2$,¹² where the same number of H_2 equivalents was produced and the same working temperature was recorded.

Kinetics laws and parameters for the better-performing catalyst (1) were also calculated through volumetric measurements over time. Initial rate experiments performed at different AB concentrations and also at variable catalyst concentrations (Figures S6 and S7, SI) showed that the overall reaction is first-order in both $[\text{AB}]$ and $[\text{I}]$: $-\text{d}[\text{AB}]/\text{d}t = k_{\text{obs}}[\text{AB}] = k[\text{I}][\text{AB}]$. A final k value of $6.9 \times 10^{-3} \text{ M}^{-1} \text{ s}^{-1}$ was calculated for 1 at 55 °C. Reactions of 1 with NH_3BD_3 , ND_3BH_3 , and ND_3BD_3 were carried out, in order to shed light on the kinetic isotope effect (KIE) (Table S1, SI) in the dehydrogenation catalysis. The collected data showed that a normal rate decrease with deuteration is observed, with the same extent for both N-deuteration [ND_3BH_3 ; $k_{\text{H}}/k_{\text{D}} = 2.2(1)$] and B-deuteration [NH_3BD_3 ; $k_{\text{H}}/k_{\text{D}} = 2.2(7)$]. In the fully deuterated compound ND_3BD_3 , the KIE is equal to the product of the ND and BD values (in the limit of the experimental error): $k_{\text{H}}/k_{\text{D}} = 4.5(2)$. This result suggests that both B–H and N–H activation take place during the rate-determining step (as confirmed by the DFT analysis, vide infra).²⁹ The consequent release of the inorganic ethylene analogue $\text{BH}_2=\text{NH}_2$ in the reaction environment as an intermediate was confirmed experimentally through the observation of $\text{H}_2\text{N}-\text{BCy}_2$ in the $^{11}\text{B}\{^1\text{H}\}$ NMR spectrum of the reaction mixture upon dehydrogenation in the presence of cyclohexene (Figure S8, SI), according to a well-established trapping protocol developed by Baker and co-workers.²⁸ The solution retains a bright-red color during the catalysis, and the addition of mercury does not modify the reaction rate in the limit of the experimental error (Figure S9, SI). This is consistent with a homogeneous process. As for 2, no $\text{H}_2\text{N}-\text{BCy}_2$ could be found in the $^{11}\text{B}\{^1\text{H}\}$ NMR spectra

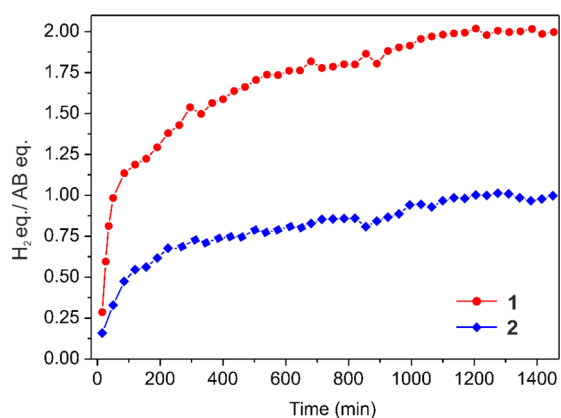


Figure 2. H_2 equivalents vs time kinetic profiles of 1 and 2 in their reaction with AB (1:3 stoichiometric ratio, THF, $T = 55$ °C).

when the catalysis is carried out in the presence of cyclohexene (Figure S10, SI), thus confirming Paul's classification described above.²⁸

Reactions with NH Acids. VT-FTIR Monitoring of the DHB Interaction. The interaction of complexes **1** and **2** with AB and DMAB was investigated by VT-FTIR (−40 to 0 °C) in toluene (DMAB) and THF (AB) solutions. In toluene, the region of the CoH stretching vibrations is hidden by the solvent overtones. Thus, the reaction was followed only by monitoring the NH and BH stretching regions of the amine borane of choice.

Initially, the stoichiometric mixture of **1** and DMAB was taken into account. Under these conditions, a new $\nu_{\text{NH}}^{\text{bond}}$ band appeared at 3133 cm^{-1} , 136 cm^{-1} below that of free DMAB (Figure 3a), indicating NH⋯HCo dihydrogen bond forma-

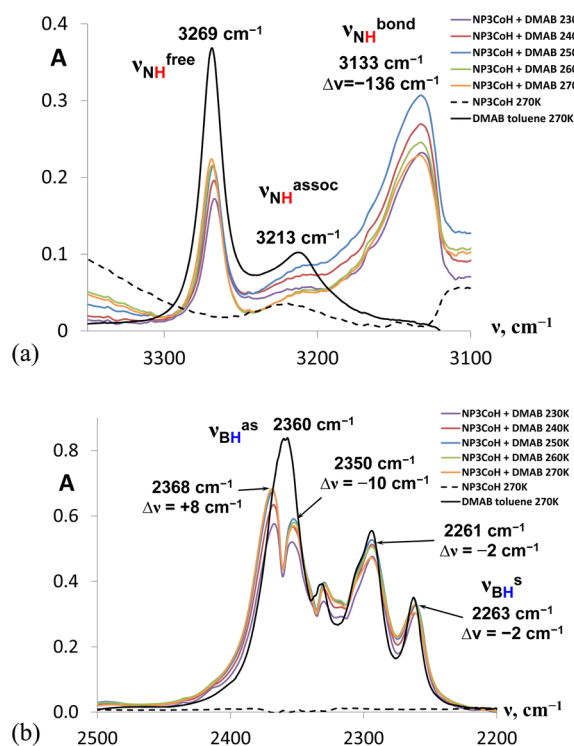


Figure 3. VT-FTIR spectra of DMAB at −83 °C (0.064 M, black solid line) and **1** at 0 °C (0.064 M, black dashed line) and in the presence 1 mol equiv of DMAB in the ν_{NH} region (a) and in the ν_{BH} region (b) in toluene (−83 to −13 °C); $l = 1$ mm.

tion.³⁰ Simultaneously, the desymmetrization of $\text{BH}_{\text{term}}^{\text{as}}$ bands occurs in the region of BH stretching vibrations: two new bands appear at 2368 cm^{-1} ($\Delta\nu = +8 \text{ cm}^{-1}$) and 2350 cm^{-1} ($\Delta\nu = -10 \text{ cm}^{-1}$) instead of one $\text{BH}_{\text{term}}^{\text{as}}$ band at 2360 cm^{-1} and a shoulder at 2261 cm^{-1} ($\Delta\nu = -2 \text{ cm}^{-1}$) (Figure 3b). Such changes can be the consequence of a weak $\text{BH}\cdots\text{Co}$ interaction.³¹ However, this spectral range is rather complicated to analyze, due to the overlap of ν_{BH} bands with the δ_{BH} bending vibration overtones^{30,31} as well as with the $^{10}\text{B-H}$ stretching vibrations³² that fall at higher wavenumbers than those of $^{11}\text{B-H}$ and induce a band broadening.

In order to reproduce the experimental catalytic conditions, the IR spectra of complexes **1** and **2** were measured in THF at $T = +55$ °C in the presence of 3 equiv of AB. A new $\nu_{\text{CoH}}^{\text{bond}}$ band of the $\text{CoH}\cdots\text{HN}$ DHB adduct appeared at a lower frequency^{30,33} (Figure 4a; $\Delta\nu_{\text{CoH}} = -17$ and -14 cm^{-1} for **1**

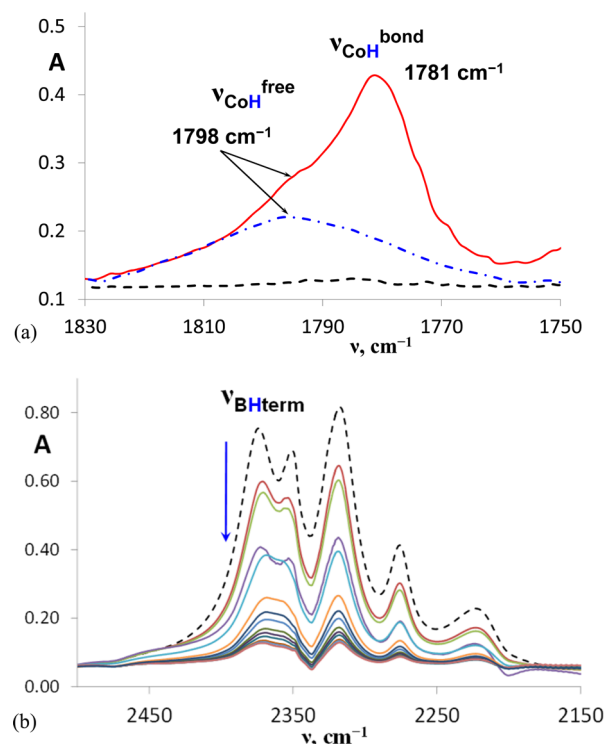


Figure 4. (a) FTIR spectra in the ν_{CoH} region of **1** (0.022 M, blue dashed-dotted line), AB (0.066 M, black dashed line), and their 1:3 mixture after 1 h of reaction (red solid line) (THF; $T = 55$ °C; $l = 1$ mm). (b) Time evolution of FTIR spectra in the ν_{BH} region of **1** (0.022 M):AB (0.066 M) = 1:3 mixture and AB (0.066 M, black dashed line) (THF; $T = 55$ °C; $l = 1$ mm). Total reaction time: 1 h. Spectra were recorded every 2–5 min.

and **2**, respectively). The intensity of both ν_{CoH} bands remained almost unchanged, whereas a gradual intensity decrease during the reaction was observed for the ν_{NH} and ν_{BH} bands of free AB (Figure 4b). These observations are in line with the involvement of Co–H bonds of **1** or **2** in the interaction with AB, which is further supported by DFT calculations (vide infra).

DFT Analysis of the AB Dehydrogenation Process. The interaction of **1** and **2** with AB has been simulated through DFT modeling. For the sake of simplicity and shorter computational times, the phenyl rings on the P atoms of the real EP_3 ligand on the catalysts have been replaced with simple hydrogen atoms [$\text{E}(\text{CH}_2\text{CH}_2\text{PH}_2)_3$, $^{\text{H}}\text{EP}_3$]. This simplification does not cause any change in the Mulliken atomic charges on the hydrides and on the cobalt atom, as confirmed by an independent optimization carried out on the real structures of **1** and **2** with the same computational set. Therefore, it is expected that the reactivity trend of ($^{\text{H}}\text{NP}_3$)Co(H) (**1_H**) and of ($^{\text{H}}\text{PP}_3$)Co(H) (**2_H**) is similar to that of **1** and **2**, respectively.

The validity of the DFT functional and basis set/pseudopotential employed in the theoretical analysis has been benchmarked against the Gibbs energy of TS_1 in the one-step AB dehydrogenation mediated by **1_H** (vide infra). For this reaction, an overall $\Delta G^\ddagger(\text{THF})$ value of 30.2 kcal mol^{-1} has been calculated, taking as the zero energy value the isolated reagents **1_H** and AB in THF (see Scheme 6 below). For the experimental validation, the reaction between **1** and AB has been carried out in THF at four different temperatures (40/45/50/55 °C) to infer the activation thermodynamic parameters

(ΔH^\ddagger and ΔS^\ddagger) with an Eyring plot showing the temperature dependence of the kinetic rate constant (k). The data fitting is reported in Figure S11 (SI). The experimental ΔG^\ddagger value derived from the Eyring analysis equals 21.2 kcal mol⁻¹, in good agreement with the calculated data. The difference in the absolute values may be ascribed to the different substituents on the phosphorus atoms between the real molecule and the computational model (i.e., **1** vs **1_H**).

The optimized structure of **1_H** has been put together with that of AB and the ensemble reoptimized. The adduct formation from the -NH₃ terminus of AB is endoergonic in THF ($\Delta G = +4.6$ kcal mol⁻¹). The resulting geometry **1_H**·AB is reported in Figure S12 (SI). A weakly attractive interaction between the N-H bonds of (uncoordinated) AB and both the hydride and cobalt atoms is present [optimized $d(\text{Co}-\text{H}\cdots\text{H}-\text{N}) = 2.30$ Å; $d(\text{Co}\cdots\text{H}-\text{N}) = 2.53$ Å]. Approaching AB from the -BH₃ terminus instead leads to a different adduct where AB is coordinated in a η^1 fashion through one of its B-H bonds to cobalt. At the same time, the N atom of the organic ligand detaches from the metal center and the NP₃ coordination mode changes from κ^4 to κ^3 -P,P,P: (κ^3 -P,P,P-^HNP₃)Co(H)(η^1 -BH-AB), **1_H**·AB (Figure 5). As already observed in (κ^4 -NP₃)Ru-

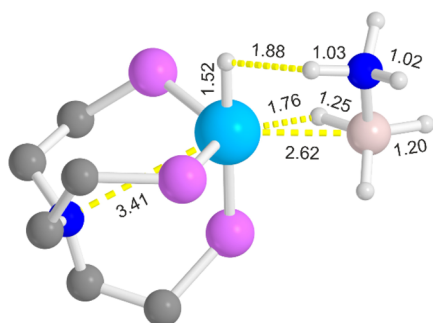


Figure 5. Optimized geometry of (κ^3 -P,P,P-^HNP₃)Co(H)(η^1 -BH-AB) (**1_H**·AB). Selected optimized bond lengths reported (Å). DHB and BH-agostic interaction depicted with yellow dotted lines. H atoms on NP₃ omitted for clarity. Atom color code: white, H; gray, C; purple, P; blue, N; pink, B; light blue, Co.

(H)₂¹² and in (κ^4 -NP₃)Ir(H)₃,³⁴ the NP₃ coordination flexibility plays a key role in this catalysis. Similarly to the previous case, the **1_H**·AB adduct formation is also endoergonic ($\Delta G = +14.3$ kcal mol⁻¹). In the calculated structure, there is an intramolecular DHB between the hydride ligand and one N-H bond [optimized $d(\text{Co}-\text{H}\cdots\text{H}-\text{N}) = 1.88$ Å]. The partial activation of the bridging B-H bond on cobalt is witnessed by its elongation with respect to the noncoordinated B-H bonds [optimized $d(\text{B}-\text{H})$: 1.25 vs 1.20 Å, respectively].

At this stage, the H₂ evolution from the DHB and concomitant loss of the “inorganic ethylene analogue” BH₂=NH₂ occurs; the transition state (**TS₁**, Figure 6) for this transformation is located 15.9 kcal mol⁻¹ above the reagents. The reaction is downhill ($\Delta G = -4.2$ kcal mol⁻¹), and **1_H** is regenerated to start a new catalytic cycle. Scheme 3 illustrates the overall catalytic cycle; the $G(\text{THF})$ vs reaction coordinate profile is reported in Scheme 6. Following this mechanism, a simultaneous B-H and N-H activation takes place, in line with the KIE experimental results. The presence of BH₂=NH₂ has also been confirmed by the trapping experiment with cyclohexene (vide supra).

The same computational approach has been followed in the case of **2_H**. The only interaction of **2_H** with AB is a simple Co-

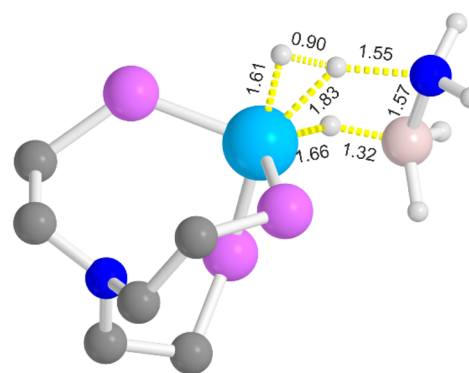
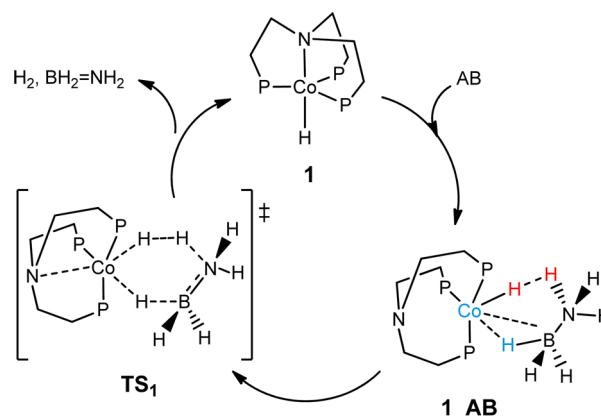


Figure 6. Optimized geometry of **TS₁**. Selected optimized bond lengths reported (Å). The bonds involved in the transformation are drawn in yellow dotted lines. H atoms on NP₃ omitted for clarity. Atom color code: see caption of Figure 5.

Scheme 3. Proposed Catalytic Cycle of AB Dehydrogenation Mediated by **1**



H \cdots H-N dihydrogen bond in the ensemble **2_H**·AB [optimized $d(\text{Co}-\text{H}\cdots\text{H}-\text{N}) = 2.17$ Å, Figure 7]. An additional (weak) interaction between the N-H bond and the metal atom is also present [optimized $d(\text{Co}\cdots\text{H}-\text{N}) = 2.51$ Å]. The Mulliken negative charges are higher on the cobalt center [$q(\text{H}) = -0.09$ e; $q(\text{Co}) = -0.77$ e]. No stable geometry with a coordinated AB could be found, at the computational level used. At odds with ^HNP₃, ^HPP₃ does not show any κ^3 -P,P,P coordination

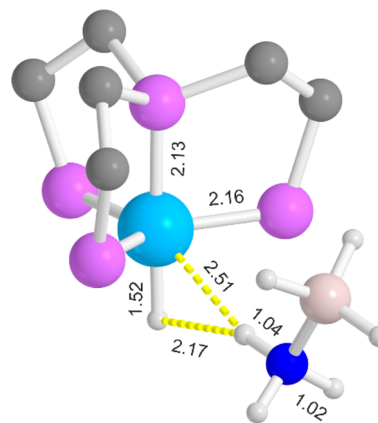


Figure 7. Optimized geometry of **2_H**·AB. Selected optimized bond lengths reported (Å). DHB depicted with yellow dotted lines. H atoms on PP₃ omitted for clarity. Atom color code: see caption of Figure 5.

mode. The apical P atom in ${}^{\text{H}}\text{PP}_3$ is more basic than the corresponding N atom in ${}^{\text{H}}\text{NP}_3$, and no detachment from the metal center is observed. Similarly to what was previously observed for 1_{H} , the $2_{\text{H}}\cdot\text{AB}$ adduct formation is endoergonic ($\Delta G = +16.2 \text{ kcal mol}^{-1}$).

The evolution of the Co–H \cdots H–N DHB from $2_{\text{H}}\cdot\text{AB}$ eventually leads to H_2 formation and to the amidoborane complex (${}^{\text{H}}\text{PP}_3$)Co(NH $_2$ BH $_3$) (3_{H} , Figure 8). Metal proto-

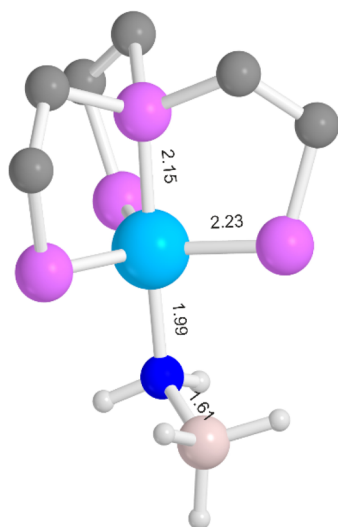


Figure 8. Optimized geometry of 3_{H} . Selected optimized bond lengths reported (Å). H atoms on PP_3 omitted for clarity. Atom color code: see caption of Figure 5.

nation may also occur while moving along the $d(\text{Co}-\text{H}\cdots\text{H}-\text{N})$ reaction coordinate, because of the high negative charge on the metal itself. The product would be the ionic species [${}^{\text{H}}\text{PP}_3$]Co(H $_2$)[NH $_2$ BH $_3$] (Scheme 4). The creation of an ion pair from two neutral reagents is always a highly unfavorable process. The corresponding transition state cannot be found on the potential energy surface, even if the geometry optimizations are carried out in THF. A free energy scan made along the $d(\text{N}-\text{H}\cdots\text{H}-\text{Co})$ reaction coordinate gives a $\Delta E^{\ddagger}(\text{THF})$ estimation of ca. 28 kcal mol $^{-1}$ for this step, at $d(\text{H}\cdots\text{H}) = 0.7 \text{ \AA}$. The classical bis(hydride) quickly releases H_2 , given the easy $\text{Co}(\text{H})_2 \leftrightarrow \text{Co}(\eta^2\text{-H}_2)$ interconversion observed for this cation.³⁵ Finally, 3_{H} is the stable product. Thermodynamics for $2_{\text{H}}\cdot\text{AB} \rightarrow 3_{\text{H}} + \text{H}_2$ provides $\Delta G = -3.5 \text{ kcal mol}^{-1}$. A similar reaction path was postulated in the nonclassical ruthenium cationic hydride [$(\kappa^4\text{-NP}_3)\text{Ru}(\text{H})(\eta^2\text{-H}_2)$] $^+$, with formation of the related amidoborane complex [$(\text{NP}_3)\text{Ru}(\text{NH}_2\cdot\text{BH}_3)(\eta^2\text{-H}_2)$] $^+$ after H_2 release.¹²

From 3_{H} , a chain growth on the coordinated amidoborane substituent can be envisaged, since the final dehydrogenation products observed experimentally are long-chain poly(aminoboranes) $[\text{BH}_2\text{NH}_2]_n$. At odds with the proposed mechanism of poly(aminoboranes) chain growth reported in the literature for the iridium hydrides (POCOP)IrH $_2$ ³⁶ or $[\text{Ir}(\text{PCy}_3)_2\text{H}_2(\eta^2\text{-H}_2)_2]^+$,³⁷ no $\text{BH}_2=\text{NH}_2$ insertion in the Co–N bond or further AB coordination to the metal center can be postulated here, since the experimental evidence is against this hypothesis. A plausible chain growth mechanism in agreement with the collected data is that proposed by Li and co-workers in 2010.³⁸ In this paper, AB dissociation into free BH_3 and NH_3 is postulated. The B–N bond cleavage is faster than the direct intermolecular H_2 production from the reaction between two AB monomers. The AB dissociation energy in THF (calculated as $-\Delta G_f$ from NH_3 and BH_3 at the M06//6-311++G** computational level) is 23.9 kcal mol $^{-1}$. Following this idea, it is reasonable to think about sequential reaction steps of 3_{H} with borane and ammonia. BH_3 and NH_3 coordination to the cobalt center in 3_{H} has been analyzed computationally. While ammonia coordination is unfeasible (the metal center is highly nucleophilic in 2_{H} , as witnessed by its negative atomic charge; therefore, its interaction with the nitrogen lone pair on NH_3 is repulsive), the electrophilic borane forms instead a stable adduct: *cis*-(${}^{\text{H}}\text{PP}_3$)Co(BH_3)(NH $_2$ BH $_3$) (3_{H}-BH_3 , Figure 9).

From 3_{H} , a chain growth on the coordinated amidoborane substituent can be envisaged, since the final dehydrogenation products observed experimentally are long-chain poly(aminoboranes) $[\text{BH}_2\text{NH}_2]_n$. At odds with the proposed mechanism of poly(aminoboranes) chain growth reported in the literature for the iridium hydrides (POCOP)IrH $_2$ ³⁶ or $[\text{Ir}(\text{PCy}_3)_2\text{H}_2(\eta^2\text{-H}_2)_2]^+$,³⁷ no $\text{BH}_2=\text{NH}_2$ insertion in the Co–N bond or further AB coordination to the metal center can be postulated here, since the experimental evidence is against this hypothesis. A plausible chain growth mechanism in agreement with the collected data is that proposed by Li and co-workers in 2010.³⁸ In this paper, AB dissociation into free BH_3 and NH_3 is postulated. The B–N bond cleavage is faster than the direct intermolecular H_2 production from the reaction between two AB monomers. The AB dissociation energy in THF (calculated as $-\Delta G_f$ from NH_3 and BH_3 at the M06//6-311++G** computational level) is 23.9 kcal mol $^{-1}$. Following this idea, it is reasonable to think about sequential reaction steps of 3_{H} with borane and ammonia. BH_3 and NH_3 coordination to the cobalt center in 3_{H} has been analyzed computationally. While ammonia coordination is unfeasible (the metal center is highly nucleophilic in 2_{H} , as witnessed by its negative atomic charge; therefore, its interaction with the nitrogen lone pair on NH_3 is repulsive), the electrophilic borane forms instead a stable adduct: *cis*-(${}^{\text{H}}\text{PP}_3$)Co(BH_3)(NH $_2$ BH $_3$) (3_{H}-BH_3 , Figure 9).

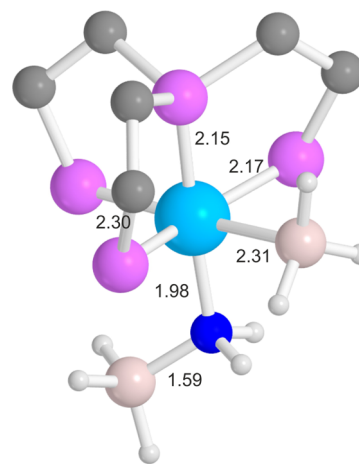
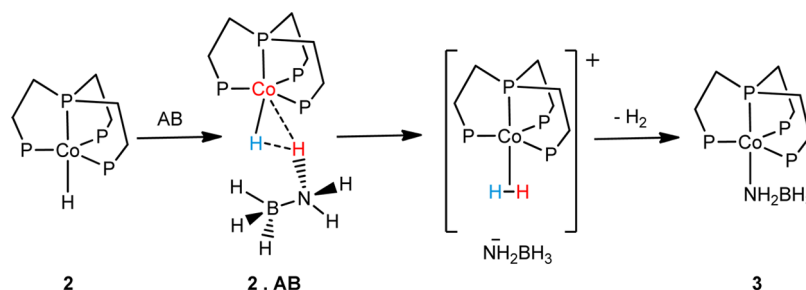


Figure 9. Optimized geometry of 3_{H}-BH_3 . Selected optimized bond lengths reported (Å). H atoms on PP_3 omitted for clarity. Atom color code: see caption of Figure 5.

Scheme 4. Proposed Formation of Species 3 from 2 + AB: Metal Protonation, Dihydride–Dihydrogen Cationic Complex Tautomerization, and H_2 Release



ΔG for this step equals $-7.1 \text{ kcal mol}^{-1}$. The coordination geometry on cobalt is now octahedral; the borane and amidoborane ligands are in a *cis* disposition. The Co–P bond *trans* to BH_3 is longer than the others [optimized $d(\text{Co–P}) = 2.30$ vs 2.17 \AA , respectively], because of the *trans* effect of the electrophilic boron atom weakening the Co–P interaction.

From this species, a transition state of borane insertion in the Co–N bond has been found (TS_2 , Figure 10), lying at 33.0 kcal

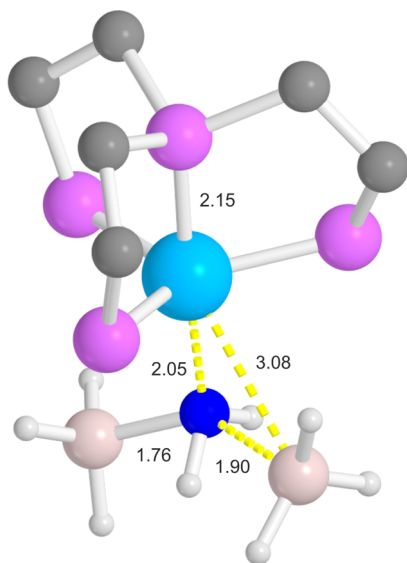


Figure 10. Optimized geometry of TS_2 . Selected optimized bond lengths reported (\AA). The bonds involved in the transformation are drawn in yellow dotted lines. H atoms on PP_3 omitted for clarity. Atom color code: see caption of Figure 5.

mol^{-1} above 3_{H}BH_3 . The reaction product is the “BNB” complex ($^{\text{H}}\text{PP}_3$)Co($\sigma\text{-BH-BH}_3\text{NH}_2\text{BH}_3$) (4_{H} , Figure 11). ΔG for this step equals $-15.1 \text{ kcal mol}^{-1}$. In this compound, the anionic $[\text{BH}_3\text{NH}_2\text{BH}_3]^-$ chain is coordinated to the cobalt ion in a $\sigma\text{-BH}$ agostic fashion. The B–H bond involved in the

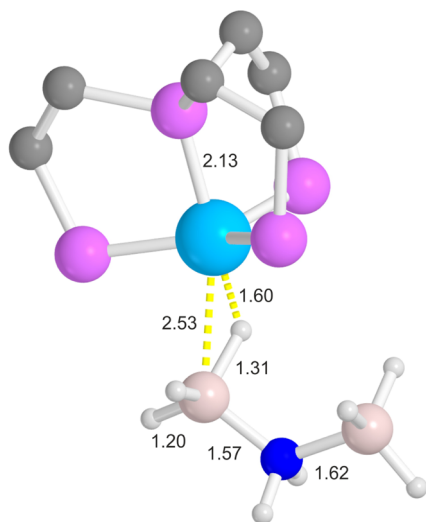
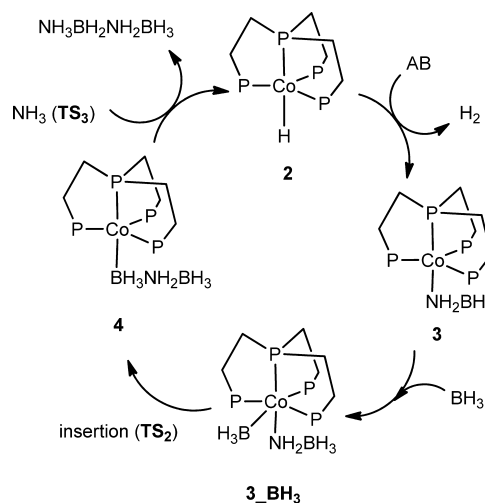


Figure 11. Optimized geometry of 4_{H} . Selected optimized bond lengths reported (\AA). $\sigma\text{-BH}$ -agostic bond drawn in yellow dotted lines. H atoms on PP_3 omitted for clarity. Atom color code: see caption of Figure 5.

agostic interaction with the metal center is slightly longer than the others [optimized $d(\text{B–H}) = 1.31$ vs 1.20 \AA , respectively]. From 4_{H} , further reaction of free NH_3 with the “BNB” chain to get the “NBNB” dimer $\text{NH}_3\text{BH}_2\text{NH}_2\text{BH}_3$ and regenerate 2_{H} is the last step closing the catalytic cycle (Scheme 5). The

Scheme 5. Proposed Reaction Scheme of AB Dehydrogenation Mediated by 2: Oligomeric Chain Growth via BH_3 Insertion into the Co–N Bond (TS_2) Followed by Chain Termination and Regeneration of the Active Species through Reaction with Free NH_3 (TS_3)



corresponding transition state TS_3 has been located at $16.7 \text{ kcal mol}^{-1}$ above the reagents (Figure 12). ΔG for the $4_{\text{H}}\cdots\text{NH}_3 \rightarrow$

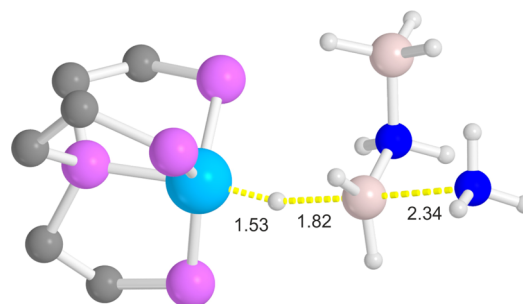
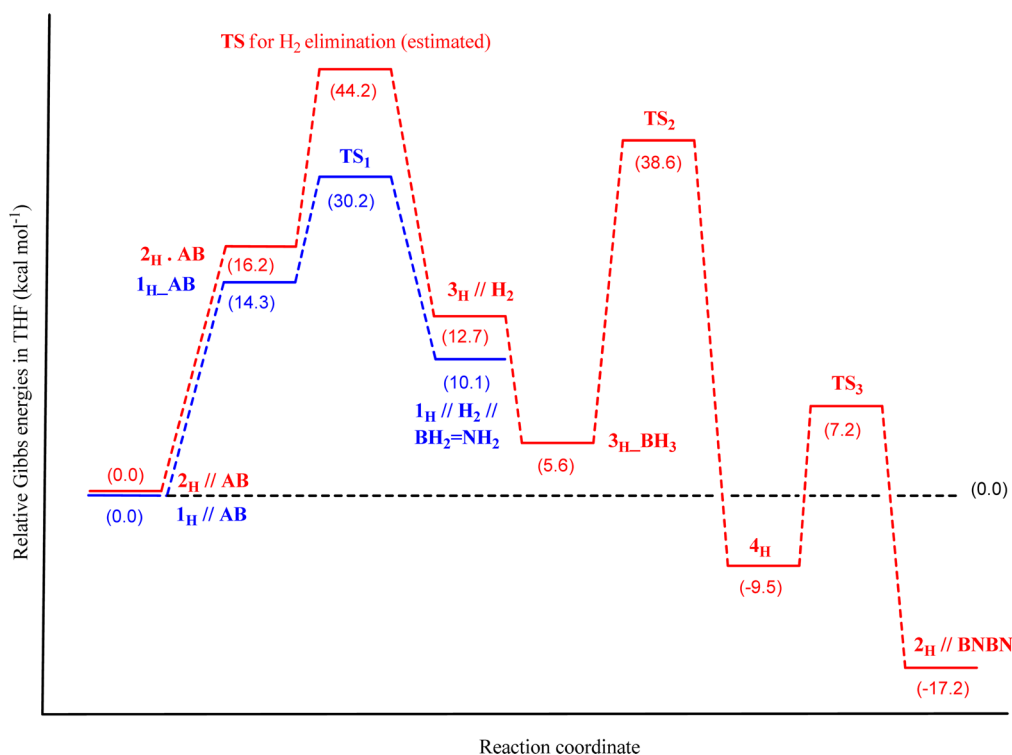


Figure 12. Optimized geometry of TS_3 . Selected optimized bond lengths reported (\AA). The bonds involved in the transformation are drawn in yellow dotted lines. H atoms on PP_3 omitted for clarity. Atom color code: see caption of Figure 5.

$2_{\text{H}}\cdots\text{NBNB}$ reaction equals $-7.7 \text{ kcal mol}^{-1}$. The complete $G(\text{THF})$ vs reaction coordinate profile is reported in Scheme 6. Overall, the highest energy barrier to overcome to start the catalysis is that related to formation of the amidoborane complex 3_{H} , higher than that found for TS_1 in the NP_3 case. This justifies the sluggish reactivity and the lower H_2 production efficiency of **2** when compared with **1** under the same experimental conditions.

CONCLUSIONS

Two cobalt(I) hydrides, $(\kappa^4\text{-EP}_3)\text{Co}(\text{H})$ ($\text{E} = \text{N}, \text{P}$), have been shown to be homogeneous catalysts for AB dehydrocoupling. The NP_3 species shows a higher catalytic activity when compared with its PP_3 analogue; the catalytic performance of

Scheme 6. Comparison of the Gibbs Energy (THF) vs Reaction Coordinate Profiles for the Two Catalysts 1_{H} (blue line) and 2_{H} (red line)

the former (in terms of H₂ equivalents per monomer equivalent produced) is the best known to date for a cobalt-containing catalyst.⁹ The spent fuels obtained at the end of the process are different for the two catalysts, and the computational analysis has confirmed that the underpinning mechanism is different. The coordination flexibility of the tripodal polyphosphine NP₃ (switching its hapticity from κ^4 to κ^3 -P,P,P) plays a crucial role in tuning the catalytic performance of (κ^4 -NP₃)Co(H) and in lowering the activation barrier of the dehydrogenation reaction. The PP₃ ligand in (κ^4 -PP₃)Co(H) (with a more basic apical P atom) does not possess the same degree of flexibility, and this mirrors the lesser extent of hydrogen production under the same experimental conditions. The combination of spectroscopic and computational tools has allowed for a more detailed description of the H₂ evolution process that follows DHB formation. New transition-metal complexes containing polydentate ligands are currently being scrutinized in our laboratory, with the aim of finding better-performing homogeneous catalysts for H₂ generation from AB and amine boranes.

■ ASSOCIATED CONTENT

● Supporting Information

The Supporting Information is available free of charge on the ACS Publications website at DOI: 10.1021/acs.inorgchem.6b02673.

Table S1, Figures S1–S12, and optimized geometries of the DFT model structures (Cartesian *xyz* coordinates and absolute G_{THF} energy values of $1_{\text{H}} \cdot \text{AB}$, 1_{H}-AB , TS₁, $2_{\text{H}} \cdot \text{AB}$, 3_{H} , 3_{H}-BH_3 , TS₂, 4_{H} , and TS₃ (PDF)

■ AUTHOR INFORMATION

Corresponding Authors

*A.R. e-mail: a.rossin@iccom.cnr.it.

*E.S.S. e-mail: shu@ineos.ac.ru.

ORCID

Giuliano Giambastiani: 0000-0002-0315-3286

Andrea Rossin: 0000-0002-1283-2803

Igor E. Golub: 0000-0003-4142-454X

Oleg A. Filippov: 0000-0002-7963-2806

Natalia V. Belkova: 0000-0001-9346-8208

Notes

The authors declare no competing financial interest.

■ ACKNOWLEDGMENTS

The bilateral project CNR (Italy)–RFBR (Russian Federation) 2015–2017 (RFBR grant no. 15-53-78027) and the Premiale project “Energia da fonti rinnovabili” 2010–2012 of the Italian National Research Council are acknowledged for financial support. CREA (Centro Ricerche Energia e Ambiente) in Colle Val d’Elsa (Siena, Italy) is acknowledged for computational resources. Financial support was also provided by the Russian Foundation for Basic Research (RFBR, grant nos. 14-03-00594, 16-03-00324) and by the Ministry of Education and Science of the Russian Federation (Agreement number 02.a03.0008).

■ REFERENCES

- (1) (a) Rossin, A.; Peruzzini, M. Ammonia–Borane and Amine–Borane Dehydrogenation Mediated by Complex Metal Hydrides. *Chem. Rev.* **2016**, *116*, 8848–8872. (b) Yadav, M.; Xu, Q. Liquid-phase chemical hydrogen storage materials. *Energy Environ. Sci.* **2012**, *5*, 9698–9725. (c) Demirci, U. B.; Miele, P. Chemical hydrogen storage: ‘material’ gravimetric capacity versus ‘system’ gravimetric capacity. *Energy Environ. Sci.* **2011**, *4*, 3334–3341. (d) Jiang, H.-L.; Xu, Q.

Catalytic hydrolysis of ammonia borane for chemical hydrogen storage. *Catal. Today* **2011**, *170*, 56–63. (e) Sanyal, U.; Demirci, U. B.; Jagirdar, B. R.; Miele, P. Hydrolysis of Ammonia Borane as a Hydrogen Source: Fundamental Issues and Potential Solutions Towards Implementation. *ChemSusChem* **2011**, *4*, 1731–1739. (f) Hamilton, C. W.; Baker, R. T.; Staubitz, A.; Manners, I. B–N compounds for chemical hydrogen storage. *Chem. Soc. Rev.* **2009**, *38*, 279–293.

(2) (a) Hügler, T.; Hartl, M.; Lentz, D. The Route to a Feasible Hydrogen-Storage Material: MOFs versus Ammonia Borane. *Chem. - Eur. J.* **2011**, *17*, 10184–10207. (b) Staubitz, A.; Robertson, A. P. M.; Manners, I. Ammonia-Borane and Related Compounds as Dihydrogen Sources. *Chem. Rev.* **2010**, *110*, 4079–4124. (c) Smythe, N. C.; Gordon, J. C. Ammonia Borane as a Hydrogen Carrier: Dehydrogenation and Regeneration. *Eur. J. Inorg. Chem.* **2010**, *2010*, 509–521. (d) Stephens, F. H.; Pons, V. P.; Baker, R. T. Ammonia-borane: the hydrogen source par excellence? *Dalton Trans.* **2007**, 2613–2626. (e) Marder, T. B. Will We Soon Be Fueling our Automobiles with Ammonia-Borane? *Angew. Chem., Int. Ed.* **2007**, *46*, 8116–8118.

(3) The following are some selected examples, grouped according to the metal type. Ruthenium: (a) Wallis, C. J.; Dyer, H.; Vendier, L.; Alcaraz, G.; Sabo-Etienne, S. Dehydrogenation of Diamine-Monoboranes to Cyclic Diaminoboranes: Efficient Ruthenium-Catalyzed Dehydrogenative Cyclization. *Angew. Chem., Int. Ed.* **2012**, *51*, 3646–3648. (b) Conley, B. L.; Guess, D.; Williams, T. J. A Robust, Air-Stable, Reusable Ruthenium Catalyst for Dehydrogenation of Ammonia Borane. *J. Am. Chem. Soc.* **2011**, *133*, 14212–14215. (c) Alcaraz, G.; Sabo-Etienne, S. Coordination and Dehydrogenation of Amine-Boranes at Metal Centers. *Angew. Chem., Int. Ed.* **2010**, *49*, 7170–7179. (d) Conley, B. L.; Williams, T. J. Dehydrogenation of Ammonia-Borane by Shvo's Catalyst. *Chem. Commun.* **2010**, *46*, 4815–4817. (e) Käb, M.; Friedrich, A.; Drees, M.; Schneider, S. Ruthenium complexes with cooperative PNP ligands: bifunctional catalysts for the dehydrogenation of ammonia-borane. *Angew. Chem., Int. Ed.* **2009**, *48*, 905–907. (f) Blaquiére, N.; Diallo-Garcia, S.; Gorelsky, S. I.; Black, D. A.; Fagnou, K. Ruthenium-Catalyzed Dehydrogenation of Ammonia Boranes. *J. Am. Chem. Soc.* **2008**, *130*, 14034–14035. Rhodium: Sewell, L. J.; Lloyd-Jones, G. C.; Weller, A. S. Development of a Generic Mechanism for the Dehydrocoupling of Amine-Boranes: A Stoichiometric, Catalytic, and Kinetic Study of H_3B-NMe_2H Using the $[Rh(PCy_3)_2]^+$ Fragment. *J. Am. Chem. Soc.* **2012**, *134*, 3598–3610. Tang, C. Y.; Thompson, A. L.; Aldridge, S. Rhodium and Iridium Aminoborane Complexes: Coordination Chemistry of BN Alkene Analogues. *Angew. Chem., Int. Ed.* **2010**, *49*, 921–925. Alcaraz, G.; Chaplin, A. B.; Stevens, C. J.; Clot, E.; Vendier, L.; Weller, A. S.; Sabo-Etienne, S. Ruthenium, Rhodium, and Iridium Bis(σ -B–H) Diisopropylaminoborane Complexes. *Organometallics* **2010**, *29*, 5591–5595. Chaplin, A. B.; Weller, A. S. B–H Activation at a Rhodium(I) Center: Isolation of a Bimetallic Complex Relevant to the Transition-Metal-Catalyzed Dehydrocoupling of Amine-Boranes. *Angew. Chem., Int. Ed.* **2010**, *49*, 581–584. Dallanegra, R.; Chaplin, A. B.; Weller, A. S. Bis(σ -amine-borane) Complexes: An Unusual Binding Mode at a Transition-Metal Center. *Angew. Chem., Int. Ed.* **2009**, *48*, 6875–6878. Douglas, T. M.; Chaplin, A. B.; Weller, A. S.; Yang, X.; Hall, M. B. Monomeric and Oligomeric Amine-Borane σ -Complexes of Rhodium. Intermediates in the Catalytic Dehydrogenation of Amine-Boranes. *J. Am. Chem. Soc.* **2009**, *131*, 15440–15456. Douglas, T. M.; Chaplin, A. B.; Weller, A. S. Amine-Borane σ -Complexes of Rhodium. Relevance to the Catalytic Dehydrogenation of Amine-Boranes. *J. Am. Chem. Soc.* **2008**, *130*, 14432–14433. Chen, Y.; Fulton, J. L.; Linehan, J. C.; Autrey, T. In Situ XAFS and NMR Study of Rhodium-Catalyzed Dehydrogenation of Dimethylamine Borane. *J. Am. Chem. Soc.* **2005**, *127*, 3254–3255. Iridium: Johnson, H. C.; Robertson, A. P. M.; Chaplin, A. B.; Sewell, L. J.; Thompson, A. L.; Haddow, M. F.; Manners, I. A.; Weller, A. S. Catching the First Oligomerization Event in the Catalytic Formation of Polyaminoboranes: $H_3B-NMe_2-NMe_2$ Bound to Iridium. *J. Am. Chem. Soc.* **2011**, *133*, 11076–11079. Rossin, A.; Caporali, M.; Gonsalvi, L.; Guerri, A.; Lledós, A.; Peruzzini, M.; Zanolini, F.

Selective B–H versus N–H Bond Activation in Ammonia Borane by $[Ir(dppm)_2]OTf$. *Eur. J. Inorg. Chem.* **2009**, *2009*, 3055–3059. Paul, A.; Musgrave, C. B. Catalyzed Dehydrogenation of Ammonia-Borane by Iridium Dihydrogen Pincer Complex Differs from Ethane Dehydrogenation. *Angew. Chem., Int. Ed.* **2007**, *46*, 8153–8156. Denney, M. C.; Pons, V.; Hebden, T. J.; Heinekey, M.; Goldberg, K. I. Efficient Catalysis of Ammonia Borane Dehydrogenation. *J. Am. Chem. Soc.* **2006**, *128*, 12048–12049. Palladium: Rossin, A.; Bottari, G.; Lozano-Vila, A.; Paneque, M.; Peruzzini, M.; Rossi, A.; Zanolini, F. Catalytic Amine-Borane Dehydrogenation by a PCP-pincer Palladium Complex: a Combined Experimental and DFT Analysis of the Reaction Mechanism. *Dalton Trans.* **2013**, *42*, 3533–3541. Kim, S.-K.; Han, W.-S.; Kim, T.-J.; Kim, T.-Y.; Nam, S. W.; Mitoraj, M.; Piekó, L.; Michalak, A.; Hwang, S.-J.; Kang, S. O. Palladium Catalysts for Dehydrogenation of Ammonia Borane with Preferential B–H Activation. *J. Am. Chem. Soc.* **2010**, *132*, 9954–9955.

(4) (a) Helten, H.; Dutta, B.; Vance, J. R.; Sloan, M. E.; Haddow, M. F.; Sproules, S.; Collison, D.; Whittell, G. R.; Lloyd-Jones, G. C.; Manners, I. Paramagnetic Titanium(III) and Zirconium(III) Metallocene Complexes as Precatalysts for the Dehydrocoupling/Dehydrogenation of Amine-Boranes. *Angew. Chem., Int. Ed.* **2013**, *52*, 437–440. (b) Sloan, M. E.; Staubitz, A.; Clark, T. J.; Russell, C. A.; Lloyd-Jones, G.; Manners, I. Homogeneous Catalytic Dehydrocoupling/Dehydrogenation of Amine-Borane Adducts by Early Transition Metal, Group 4 Metallocene Complexes. *J. Am. Chem. Soc.* **2010**, *132*, 3831–3841. (c) Clark, T. J.; Russell, C. A.; Manners, I. Homogeneous, Titanocene-Catalyzed Dehydrocoupling of Amine-Borane Adducts. *J. Am. Chem. Soc.* **2006**, *128*, 9582–9583.

(5) Kawano, Y.; Uruichi, M.; Shimoi, M.; Taki, S.; Kawaguchi, T.; Kakizawa, T.; Ogino, H. Dehydrocoupling Reactions of Borane-Secondary and -Primary Amine Adducts Catalyzed by Group-6 Carbonyl Complexes: Formation of Aminoboranes and Borazines. *J. Am. Chem. Soc.* **2009**, *131*, 14946–14957.

(6) Muhammad, S.; Moncho, S.; Brothers, E. N.; Bengali, A. A. Dehydrogenation of a Tertiary Amine-Borane by a Rhenium Complex. *Chem. Commun.* **2014**, *50*, 5874–5877.

(7) (a) Kalviri, H. A.; Gärtner, F.; Ye, G.; Korobkov, I.; Baker, R. T. Probing the Second Dehydrogenation Step in Ammonia-Borane Dehydrocoupling: Characterization and Reactivity of the Key Intermediate, B-(cyclotriborazanyl)amine-borane. *Chem. Sci.* **2015**, *6*, 618–624. (b) Bhattacharya, P.; Krause, J. A.; Guan, H. Mechanistic Studies of Ammonia Borane Dehydrogenation Catalyzed by Iron Pincer Complexes. *J. Am. Chem. Soc.* **2014**, *136*, 11153–11161. (c) Baker, R. T.; Gordon, J. C.; Hamilton, C. W.; Henson, N. J.; Lin, P.-H.; Maguire, S.; Murugesu, M.; Scott, B. L.; Smythe, N. C. Iron Complex-Catalyzed Ammonia-Borane Dehydrogenation. A Potential Route toward B–N-Containing Polymer Motifs Using Earth-Abundant Metal Catalysts. *J. Am. Chem. Soc.* **2012**, *134*, 5598–5609.

(8) (a) Vogt, M.; de Bruin, B.; Berke, H.; Trincado, M.; Grützmacher, H. Amino Olefin Nickel(I) and Nickel(0) Complexes as Dehydrogenation Catalysts for Amine Boranes. *Chem. Sci.* **2011**, *2*, 723–727. (b) Keaton, R. J.; Blacquiére, J. M.; Baker, R. T. Base Metal Catalyzed Dehydrogenation of Ammonia-Borane for Chemical Hydrogen Storage. *J. Am. Chem. Soc.* **2007**, *129*, 1844–1845.

(9) Lin, T.-P.; Peters, J. C. Boryl-Mediated Reversible H_2 Activation at Cobalt: Catalytic Hydrogenation, Dehydrogenation, and Transfer Hydrogenation. *J. Am. Chem. Soc.* **2013**, *135*, 15310–15313.

(10) (a) Palacios, M. D.; Puerta, M. C.; Valerga, P.; Lledós, A.; Veilly, E. Coordinatively Unsaturated Semisandwich Complexes of Ruthenium with Phosphinoamine Ligands and Related Species: A Complex Containing (R,R)-1,2-Bis((diisopropylphosphino)amino)cyclohexane in a New Coordination Form $\kappa^3P,P',N-\eta^2-P,N$. *Inorg. Chem.* **2007**, *46*, 6958–6967. (b) Bertolasi, V.; Bianchini, C.; de los Ríos, I.; Marvelli, L.; Peruzzini, M.; Rossi, R.; Marchi, A. Rhenium(III) and Rhenium(V) Complexes Stabilized by the Potentially Tetradentate Ligand Tris(2-diphenylphosphinoethyl)amine. *Inorg. Chim. Acta* **2002**, *327*, 140–146. (c) Mealli, C.; Ghilardi, C. A.; Orlandini, A. Structural Flexibility and Bonding Capabilities of the Ligand NP_3 Toward the Transition Metals. *Coord. Chem. Rev.* **1992**, *120*, 361–387. (d) Morassi, R.;

- Bertini, I.; Sacconi, L. Five-Coordination in Iron(II); Cobalt(II) and Nickel(II) Complexes. *Coord. Chem. Rev.* **1973**, *11*, 343–402.
- (e) Sacconi, L. The Influence of Geometry and Donor-Atom Set on the Spin State of Five-Coordinate Cobalt (II) and Nickel (II) Complexes. *Coord. Chem. Rev.* **1972**, *8*, 351–367.
- (11) Bianchini, C.; Meli, A.; Peruzzini, M.; Vizza, F.; Zanolini, F. Tripodal Polyphosphine Ligands Control Selectivity of Organometallic Reactions. *Coord. Chem. Rev.* **1992**, *120*, 193–208.
- (12) Rossin, A.; Rossi, A.; Peruzzini, M.; Zanolini, F. Chemical Hydrogen Storage: Ammonia Borane Dehydrogenation Catalyzed by NP_3 Ruthenium Hydrides ($\text{NP}_3=\text{N}(\text{CH}_2\text{CH}_2\text{PPh}_2)_3$). *ChemPlusChem* **2014**, *79*, 1316–1325.
- (13) Sacconi, L.; Bertini, I. Low- and High-Spin Five-Coordinate Cobalt(II) and Nickel(II) Complexes with Tris(2-diphenylphosphinoethyl)amine. *J. Am. Chem. Soc.* **1968**, *90*, 5443–5446.
- (14) Sacconi, L.; Ghilardi, C. A.; Mealli, C.; Zanolini, F. Synthesis, Properties and Structural Characterization of Complexes of Cobalt and Nickel in Low Oxidation States with the Tripod Ligand Tris(2-diphenylphosphinoethyl)amine. *Inorg. Chem.* **1975**, *14*, 1380–1386.
- (15) Ghilardi, C. A.; Midollini, S.; Sacconi, L. Reactions of the Tripod Ligand Tris(2-diphenylphosphinoethyl)phosphine with Cobalt(II) and Nickel(II) Salts and Sodium Borohydride. Structural Characterization of a Five-Coordinate Cobalt(I) Hydride Complex. *Inorg. Chem.* **1975**, *14*, 1790–1795.
- (16) Hu, M. G.; Van Paasschen, J. M.; Geanangel, R. A. New Synthetic Approaches to Ammonia-Borane and its Deuterated Derivatives. *J. Inorg. Nucl. Chem.* **1977**, *39*, 2147–2150.
- (17) Frisch, M. J. et al., *Gaussian09*, Revision C.01, Gaussian Inc., Wallingford, CT, 2010.
- (18) Zhao, Y.; Truhlar, D. G. The M06 Suite of Density Functionals for Main Group Thermochemistry, Thermochemical Kinetics, Non-covalent Interactions, Excited States and Transition Elements: Two New Functionals and Systematic Testing of Four M06-class Functionals and 12 Other Functionals. *Theor. Chem. Acc.* **2008**, *120*, 215–241.
- (19) Zhao, Y.; Truhlar, D. G. Density Functionals with Broad Applicability in Chemistry. *Acc. Chem. Res.* **2008**, *41*, 157–167.
- (20) (a) Andrae, D.; Haeuessermann, U.; Dolg, M.; Stoll, H.; Preuss, H. Energy-adjusted *ab initio* Pseudopotentials for the Second and Third Row Transition Elements. *Theor. Chem. Acc.* **1990**, *77*, 123–141. (b) Dunning, T. H., Jr.; Hay, P. J. In *Modern Theoretical Chemistry*; Schaefer, H. F., III, Ed.; Plenum: New York, 1976; Vol. 3, pp 1–28.
- (21) Lynch, B. J.; Zhao, Y.; Truhlar, D. G. Effectiveness of Diffuse Basis Functions for Calculating Relative Energies by Density Functional Theory. *J. Phys. Chem. A* **2003**, *107*, 1384–1388.
- (22) (a) Höllwarth, A.; Böhme, M.; Dapprich, S.; Ehlers, A. W.; Gobbi, A.; Jonas, V.; Köhler, K. F.; Stegmann, R.; Veldkamp, A.; Frenking, G. A Set of *d*-Polarization Functions for Pseudo-Potential Basis Sets of the Main Group Elements Al-Bi and *f*-Type Polarization Functions for Zn, Cd, Hg. *Chem. Phys. Lett.* **1993**, *208*, 237–240. (b) Ehlers, A. W.; Böhme, M.; Dapprich, S.; Gobbi, A.; Höllwarth, A.; Jonas, V.; Köhler, K. F.; Stegmann, R.; Veldkamp, A.; Frenking, G. A Set of *f*-Polarization Functions for Pseudo-Potential Basis Sets of the Transition Metals Sc-Cu, Y-Ag and La-Au. *Chem. Phys. Lett.* **1993**, *208*, 111–114.
- (23) Fukui, K. The Path of Chemical Reactions - the IRC Approach. *Acc. Chem. Res.* **1981**, *14*, 363–368.
- (24) Marenich, A. V.; Cramer, C. J.; Truhlar, D. G. Universal Solvation Model Based on Solute Electron Density and on a Continuum Model of the Solvent Defined by the Bulk Dielectric Constant and Atomic Surface Tensions. *J. Phys. Chem. B* **2009**, *113*, 6378–6396.
- (25) (a) Heinekey, D. M.; Liegeois, A.; van Roon, M. Cationic Dihydrogen Complexes of Rhodium and Cobalt: A Reinvestigation. *J. Am. Chem. Soc.* **1994**, *116*, 8388–8389. (b) Bianchini, C.; Mealli, C.; Meli, A.; Peruzzini, M.; Zanolini, F. A Stable η^2 -Dihydrogen Complex of Cobalt. Role of the Hydrogen-Hydrogen Interaction in Hydrogen Transfer from Metal to Alkene. *J. Am. Chem. Soc.* **1988**, *110*, 8725–8726.
- (26) (a) Lingam, H. K.; Wang, C.; Gallucci, J. C.; Chen, X.; Shore, S. G. New Syntheses and Structural Characterization of $\text{NH}_3\text{BH}_2\text{Cl}$ and $(\text{BH}_2\text{NH}_2)_3$ and Thermal Decomposition Behavior of $\text{NH}_3\text{BH}_2\text{Cl}$. *Inorg. Chem.* **2012**, *51*, 13430–13436. (b) Shaw, W. J.; Linehan, J. C.; Szymczak, N. K.; Heldebrant, D. J.; Yonker, C.; Camaioni, D. M.; Baker, R. T.; Autrey, T. In Situ Multinuclear NMR Spectroscopic Studies of the Thermal Decomposition of Ammonia Borane in Solution. *Angew. Chem., Int. Ed.* **2008**, *47*, 7493–7496. (c) Wang, J. S.; Geanangel, R. A. ^{11}B NMR Studies of the Thermal Decomposition of Ammonia-Borane in Solution. *Inorg. Chim. Acta* **1988**, *148*, 185–190.
- (27) Socrates, G. *Infrared and Raman Characteristic Group Frequencies: Tables and Charts*, 3rd ed.; John Wiley & Sons, 2013.
- (28) (a) Bhunya, S.; Zimmerman, P. M.; Paul, A. Unraveling the Crucial Role of Metal-Free Catalysis in Borazine and Polyborazylene Formation in Transition-Metal-Catalyzed Ammonia-Borane Dehydrogenation. *ACS Catal.* **2015**, *5*, 3478–3493. (b) Pons, V.; Baker, R. T.; Szymczak, N. K.; Heldebrant, D. J.; Linehan, J. C.; Matus, M. H.; Grant, D. J.; Dixon, D. A. Coordination of aminoborane, NH_2BH_2 , dictates selectivity and extent of H_2 release in metal-catalysed ammonia borane dehydrogenation. *Chem. Commun.* **2008**, 6597–6599.
- (29) Espenson, J. H. *Chemical Kinetics and Reaction Mechanisms*, 2nd ed.; McGraw-Hill, 1995.
- (30) (a) Golub, I. E.; Gulyaeva, E. S.; Filippov, O. A.; Dyadchenko, V. P.; Belkova, N. V.; Epstein, L. M.; Arkhipov, D. E.; Shubina, E. S. Dihydrogen Bond Intermediated Alcoholysis of Dimethylamine-Borane in Nonaqueous Media. *J. Phys. Chem. A* **2015**, *119*, 3853–3868. (b) Belkova, N. V.; Epstein, L. M.; Filippov, O. A.; Shubina, E. S. Hydrogen and Dihydrogen Bonds in the Reactions of Metal Hydrides. *Chem. Rev.* **2016**, *116*, 8545–8587. (c) Belkova, N. V.; Shubina, E. S.; Epstein, L. M. Diverse World of Unconventional Hydrogen Bonds. *Acc. Chem. Res.* **2005**, *38*, 624–631.
- (31) Titov, A. A.; Guseva, E. A.; Smol'yakov, A. F.; Dolgushin, F. M.; Filippov, O. A.; Golub, I. E.; Krylova, A. I.; Babakhina, G. M.; Epstein, L. M.; Shubina, E. S. Complexation of Trimeric Copper(I) and Silver(I) 3,5-bis(trifluoromethyl)pyrazolates with Amine-Borane. *Russ. Chem. Bull.* **2013**, *62*, 1829–1834.
- (32) Smith, J.; Seshadri, K. S.; White, D. Infrared Spectra of Matrix Isolated $\text{BH}_3\text{-NH}_3$, $\text{BD}_3\text{-ND}_3$, and $\text{BH}_3\text{-ND}_3$. *J. Mol. Spectrosc.* **1973**, *45*, 327–337.
- (33) Belkova, N. V.; Epstein, L. M.; Filippov, O. A.; Shubina, E. S. IR spectroscopy of hydrides and its application to hydrogen bonding and proton transfer studies. In *Spectroscopic Properties of Inorganic and Organometallic Compounds: Techniques, Materials and Applications*; Yarwood, J., Douthwaite, R., Duckett, S., Eds.; The Royal Society of Chemistry, 2012; Vol. 43, pp 1–28.
- (34) Rossin, A.; Gutsul, E. I.; Belkova, N. V.; Epstein, L. M.; Gonsalvi, L.; Lledós, A.; Lyssenko, K.; Peruzzini, M.; Shubina, E. S.; Zanolini, F. Mechanistic Studies on the Interaction of $[(\kappa^3\text{-P,P,P-P-NP}_3)\text{IrH}_3][\text{NP}_3 = \text{N}(\text{CH}_2\text{CH}_2\text{PPh}_2)_3]$ with HBF_4 and Fluorinated Alcohols by Combined NMR, IR, and DFT Techniques. *Inorg. Chem.* **2010**, *49*, 4343–4354.
- (35) Bianchini, C.; Mealli, C.; Peruzzini, M.; Zanolini, F. Reversible Uptake of Hydrogen and Nitrogen at Cobalt in the Solid State. Influence of the Counter Anion on the Formation of Classical Dihydride vs. Nonclassical η^2 -Dihydrogen Forms of $[(\text{PP}_3)\text{CoH}_2]^+$. *J. Am. Chem. Soc.* **1992**, *114*, 5905–5906.
- (36) Bhunya, S.; Malakar, T.; Paul, A. Unfolding the crucial role of a nucleophile in Ziegler-Natta type Ir catalyzed polyaminoborane formation. *Chem. Commun.* **2014**, *50*, 5919–5922.
- (37) Kumar, A.; Johnson, H. C.; Hooper, T. N.; Weller, A. S.; Algarra, A. G.; Macgregor, S. A. Multiple metal-bound oligomers from Ir-catalysed dehydropolymerisation of $\text{H}_3\text{B-NH}_3$ as probed by experiment and computation. *Chem. Sci.* **2014**, *5*, 2546–2553.
- (38) Li, J.; Kathmann, S. M.; Hu, H.-S.; Schenter, G. K.; Autrey, T.; Gutowski, M. Theoretical Investigations on the Formation and Dehydrogenation Reaction Pathways of $\text{H}(\text{NH}_2\text{BH}_2)_n\text{H}$ ($n = 1-4$)

Oligomers: Importance of Dihydrogen Interactions. *Inorg. Chem.* **2010**, *49*, 7710–7720.